PHOTONICS Research

Terahertz metalens of hyper-dispersion

Fen Zhao,[1,†] Ziping Li,[2,†] Sheng Li,[1] Xuemei Dai,[1] Yi Zhou,[1] Xiaoyu Liao,[2] J. C. Cao,[2]
Gaofeng Liang,[1] Zhengguo Shang,[1] Zhihai Zhang,[1] Zhongquan Wen,[1,*] Hua Li,[2,3]
and Gang Chen[1,4]

[1]*Key Laboratory of Optoelectronic Technology and Systems (Chongqing University), Ministry of Education, School of Optoelectronic Engineering,
Chongqing University, Chongqing 400044, China*
[2]*Key Laboratory of Terahertz Solid State Technology, Shanghai Institute of Microsystem and Information Technology,
Chinese Academy of Sciences, Shanghai 200050, China*
[3]*e-mail: hua.li@mail.sim.ac.cn*
[4]*e-mail: gchen1@cqu.edu.cn*
Corresponding author: wenzq@cqu.edu.cn

Chromatic optical lenses have promising applications in three-dimensional imaging, which allows fast spectral
tomography without mechanical moving parts. The scanning range of current chromatic optical lenses is limited
by their dispersion ability. The recent development in metasurfaces provides ideal blocks for optical wavefront
manipulation and dispersion engineering of artificial materials at sub-wavelength scales. Hyper-dispersive metal-
enses can be realized by utilizing dispersive meta-atoms, which have enhanced dispersion compared to regular
diffractive lenses. This is critical for increasing the imaging depth of fast spectral tomography. In this work, a
hyper-dispersive metalens is realized with a chromatic dispersion 1.76 times greater than that of a regular dif-
fractive metalens in the THz frequency range of 2.40–2.61 THz by simultaneously controlling the frequency-
dependent phase, group delay (GD), and GD dispersion of the metalens. This approach can also be extended
to other optical spectra and improve the performance of spectral tomography.   © 2022 Chinese Laser Press

https://doi.org/10.1364/PRJ.439481

1. INTRODUCTION

Due to their wavelength-dependent focal lengths, chromatic
optical lenses have been applied in three-dimensional imaging
[1,2], which allows fast spectral tomography without mechani-
cal moving parts in confocal microscopy [3–5]. Compared with
conventional refractive lenses, diffractive optical lenses have
stronger chromatic dispersion [6], which makes them particu-
larly beneficial for non-motion fast spectral tomography with
enabled optical zooming by simply switching the illumination
wavelength [7]. Moreover, diffractive optical lenses have addi-
tional advantages of low weight and thickness, and ease of
integration. However, regular diffractive lenses suffer from
low efficiency due to non-zero-order diffractions. Metasurfaces
are artificial sub-wavelength structures that can provide effi-
cient ways to manipulate the amplitude [8–11], phase
[12–16], and polarization [17–22] of electromagnetic fields.
Metasurfaces have made great progress in generating miniature
and integrated optical devices in the terahertz regime such as
high-efficiency meta-devices [23–27], multi-foci metalenses
[13,28,29], and encoding metasurfaces [30–32]. Recently,
dispersion manipulations [33–39] have also been demonstrated
in broadband achromatic metalenses with diffraction-limited

performance for visible [40–42], near-infrared [43–45], and
THz regimes [46]. Furthermore, the super-resolution achro-
matic metalens has been demonstrated with a broad bandwidth
in the THz region [47]. Meta-devices are highly chromatic, re-
sulting from two factors: dispersion arising from a periodic lat-
tice and light confinement in either a resonant or guided
manner [41]. Dispersive metasurfaces can also be used to
enhance the chromatic dispersion of diffractive metalenses,
or hyper-dispersion [43], which is critical for increasing the im-
aging depth of fast spectral tomography [7], due to an enhanced
range of tunable focal length within the same working band-
width compared with that of the regular dispersive lens. To
verify the concept, in the present work, a dielectric metalens
is proposed with enhanced chromatic dispersion in the THz
frequency range of 2.40–2.61 THz by simultaneously control-
ling the phase, group delay (GD), and GD dispersion (GDD)
through metasurfaces. Both theoretical and experimental re-
sults show an approximate 1.76 times enhancement in chro-
matic dispersion compared to a regular diffractive metalens
with the same parameters but without dispersion engineering.
This design can be extended to other multifunctional metasur-
faces [48,49] on the basis of improving the performance of
spectral tomography.

2. THEORETICAL CONSIDERATION

The chromatic dispersion of a lens is determined by its frequency-dependent phase profile $\varphi(r, \omega)$, where r is the radial coordinate on the lens, and ω is the optical angular frequency of incident light. The phase profile can be expanded into a Taylor series near a given frequency of ω_0. The coefficients of the first three terms in the Taylor series are related to the phase profile, GD, and GDD at ω_0, respectively, as given in Eq. (1), and GD and GDD are the major concerns in dispersion engineering. Engineering the frequency-dependent phase profile $\varphi(r, \omega)$, we can further enhance the dispersion of devices by carefully arranging a dispersive meta-atom at the corresponding spatial position:

$$\varphi(r, \omega) = \varphi(r, \omega_0) + \frac{\partial\varphi(r, \omega)}{\partial\omega}\bigg|_{\omega=\omega_0} (\omega - \omega_0)$$
$$+ \frac{\partial^2\varphi(r, \omega)}{2!\partial\omega^2}\bigg|_{\omega=\omega_0} (\omega - \omega_0)^2 + O(\omega^3). \quad \text{(1)}$$

The commonly used phase profile of a metalens can be described by the hyperbolic function as given in Eq. (2):

$$\varphi(r, \omega) = -\left[\sqrt{r^2 + f^2(\omega)} - f(\omega)\right]\frac{\omega}{c}, \quad \text{(2)}$$

where $f(\omega)$ is the frequency-dependent focal length, and c is the speed of light. For a prescribed $f(\omega)$, the required GD and GDD can be obtained by calculating the first-order and second-order derivatives of the frequency-dependent phase profile, i.e., $\partial\varphi(r, \omega)/\partial\omega$ and $\partial^2\varphi(r, \omega)/\partial\omega^2$, respectively.

The dispersion ability of a metalens can be classified into different categories, according to the order of the exponential dependency of the focal length on the optical angular frequency, or $f(\omega) = A\omega^n$, where A is a real constant, and n is an integer. For the case of $n = 0$, $f(\omega) = A$ implies a chromatic-free lens with a fixed focal length of A for any given ω; for the case of $n = 1$, $f(\omega) = A\omega$ gives a lens of linear dispersion; and for the case of $n > 1$, $f(\omega) = A\omega^n$ describes a lens with enhanced chromatic dispersion, or a hyper-dispersive lens, which is expected to have stronger dispersion than reported regular diffractive lenses [41,43].

In this work, a hyper-dispersive metalens is proposed with $n = 2$. The corresponding GD and GDD are expressed in Eqs. (3) and (4):

$$\frac{\partial\varphi(r, \omega)}{\partial\omega}\bigg|_{\omega=\omega_0}$$
$$= -\frac{1}{c}\left[\sqrt{r^2 + (A\omega_0^2)^2} + \frac{2A^2\omega_0^4}{\sqrt{r^2 + (A\omega_0^2)^2}} - 3A\omega_0^2\right], \quad \text{(3)}$$

$$\frac{\partial\varphi^2(r, \omega)}{\partial\omega^2}\bigg|_{\omega=\omega_0}$$
$$= -\frac{1}{c\omega_0}\left[\frac{10A^2\omega_0^4}{(r^2 + A^2\omega_0^4)^{1/2}} - \frac{4A^4\omega_0^8}{(r^2 + A^2\omega_0^4)^{3/2}} - 6A\omega_0^2\right]. \quad \text{(4)}$$

The hyper-dispersive lens has a radius of $R = 180\lambda_0$ (21.38 mm) and focal length of $f_0 = 330\lambda_0$ (39.20 mm) at a design wavelength of $\lambda_0 = 118.8$ μm, which corresponds to optical angular frequency of $\omega_0 = 15.87$ rad/ps. The working bandwidth of the lens is 10 μm within a wavelength range from 115 to 125 μm (between 2.40 and 2.61 THz). The corresponding numerical aperture of the lens is approximately 0.478, and the constant A is chosen as 155.73 μm rad^{-2} ps^2 to guarantee a focal length of f_0 at optical angular frequency of ω_0 [$f_0(\omega_0) = A\omega_0^2$]. Figures 1(a) and 1(b) plot the required GD and GDD against the radial coordinate for the case $n = 2$ (green), respectively, where GDs and GDDs for the cases of $n = 0$ (black), $n = 1$ (red), and $n = 3$ (blue) are also plotted for comparison. It is worth noting that, for hyper-dispersive lenses of $n \geq 2$, GDD shows a clear non-monotone variation, which does not exist in the literature [41], as the presented radial coordinate is less than the specific concave upward location.

Since the phase $\varphi(r, \omega) = (\omega/c) \cdot n_{\text{eff}}(\omega) \cdot H$ of the transmitted light after passing through the meta-atom is related to the effective index n_{eff} and the height H, the GD [$\partial\varphi(r, \omega)/\partial\omega$] and GDD [$\partial^2\varphi(r, \omega)/\partial\omega^2$] can be controlled by the structure dimensions and/or material used, as noted in the literature [41]. Coupled phase-shift elements are commonly employed in dispersion modulation because of their
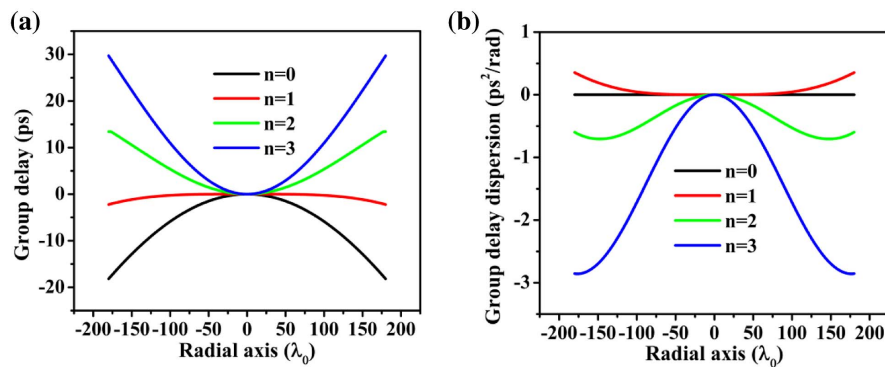
Fig. 1. Required relative (a) group delay and (b) group delay dispersion as a function of metalenses' coordinates for different orders ($n = 0$, 1, 2, and 3) of dispersion engineering. All curves are plotted based on Eqs. (3) and (4) for lenses with a focal length of $330\lambda_0$ at the designed wavelength and a radius of $180\lambda_0$.
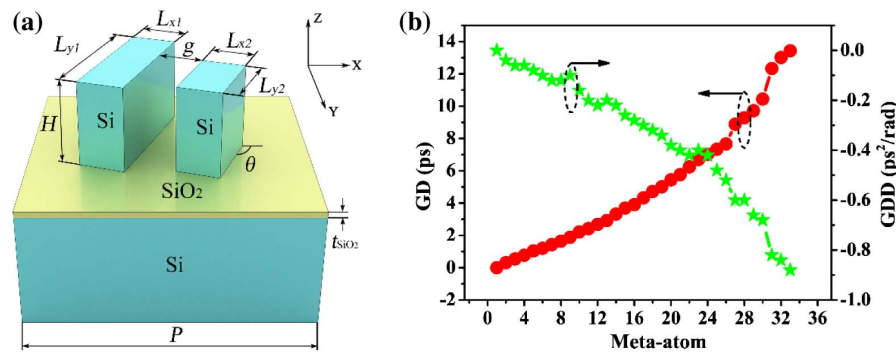
Fig. 2. (a) Schematic structure of the proposed dispersive meta-atom. The meta-atom consists of two Si blocks on a Si substrate with a SiO_2 isolation layer, and the thickness of the SiO_2 layer is $t_{SiO_2} = 2 \times$ μm. (b) Relative group delay (GD) and group delay dispersion (GDD) of the 33 optimized meta-atoms.

flexibility in dispersion engineering [50], and high-refractive-index dielectric double-strip-block meta-atoms are able to achieve a large GD range [51]. To meet the requirement of GD and GDD in the concerned wavelength range between 115 and 125 μm (i.e., between 2.40 and 2.61 THz), a family of 33 double-block Si meta-atoms was optimized by varying their geometric parameters, i.e., length L_{x1} and L_{x2}, width L_{y1} and L_{y2}, height H, pitch P, and gap width g, as shown in Fig. 2(a). Considering the maximum high-aspect ratio limited by the achievable fabrication technology, the optimized height H and pitch P are 65.7 and 66 μm, respectively, and the detailed parameters of these meta-atoms are listed in Table 1. Figure 2(b) gives the corresponding relative GD (red) and GDD (green) of the 33 meta-atoms, where the actual GD and GDD of meta-atoms were obtained by fitting the phase as a function of angular frequency with a quadratic polynomial in the concerned bandwidth. The relative value was calculated by $GD_i = GD(i) - GD(1)$ and $GDD_i = GDD(i) - GDD(1)$, where i is an integer, namely, $i = 1, 2, …, 33$. The relative GD of the 33 meta-atoms covers a range of 13.43 ps, while the relative GDD varies from 0 to –0.88 ps^2/rad, and the corresponding R-squared values [41] are greater than 0.99, indicating a high fitting degree. To compare the possible range of GDs, a relative ratio of the range of GD [$\Delta(GD)$] with respect to the period of the central wavelength of λ_0 [$\Delta(GD)/(\lambda_0/c)$] is calculated to be 33.9, which is relatively higher than that in Ref. [41]. As the range of GDDs is related to the working bandwidth of meta-atoms, they cannot be simply compared with each other. Moreover, to design other kinds of dispersive lenses with different n as illustrated in Fig. 1, specific groups of meta-atoms should be optimized.
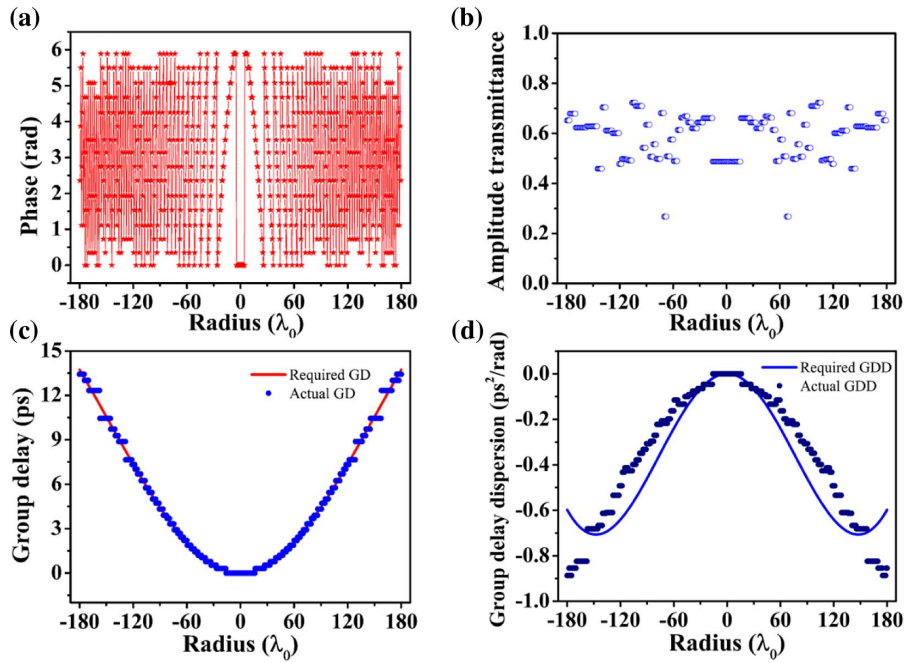
The proposed hyper-dispersive metalens was divided into 33 neighboring concentric ring-belts based on the boundaries of GD values [51]. The meta-atoms were arranged into the proper ring-belts to meet the required GD and GDD as shown in Fig. 1. The phase profile $\varphi(r, \omega_0)$ was then realized by the geometrical phase [52] through rotating the meta-atoms, namely, $\theta(r) = \varphi(r, \omega_0)/2$, where the relative phase delay between these meta-atoms has to be considered.

The transmission function and dispersion curves of the hyper-dispersive metalens are presented in Fig. 3. Figure 3(a) gives the metalens phase profile, where the red curve represents

the ideal hyperbolic phase distribution described in Eq. (1) at a wavelength of λ_0, and the red stars give the actual discrete phase distribution provided by the 33 meta-atoms. Figure 3(b) is the corresponding amplitude transmittance of the lens. The actual GD and GDD distributions of the lens are depicted in Figs. 3(c) and 3(d), respectively, where the ideal GD (red) and GDD (navy) are also plotted for comparison. Although the

Table 1. Major Parameters of Optimized Meta-Atoms (All Geometric Sizes are Given in Micrometers)

| #	L_{x1}	L_{y1}	L_{x2}	L_{y2}	g
1	21.7	26.4	11.3	32.1	8.1
2	18.9	34.9	11.3	41.5	8.1
3	15.1	26.4	17.0	32.1	11.9
4	9.4	18.9	9.4	33.9	8.1
5	9.4	20.7	9.4	33.9	8.1
6	9.4	22.6	9.4	33.9	8.1
7	9.4	41.5	9.4	41.5	8.1
8	11.3	26.4	17.0	32.1	10.0
9	21.7	26.4	9.4	33.9	8.1
10	20.7	29.2	11.3	39.6	8.1
11	17.0	39.6	9.4	41.5	8.1
12	9.4	22.6	9.4	22.6	8.1
13	17.0	39.6	9.4	30.2	8.1
14	21.7	26.4	13.2	32.1	8.1
15	21.7	26.4	19.8	32.1	8.1
16	21.7	26.4	17.0	39.6	8.1
17	17.0	39.6	19.8	30.2	8.1
18	21.7	26.4	20.7	29.2	8.1
19	15.1	43.4	11.3	45.3	8.1
20	11.3	49.0	11.3	49.0	8.1
21	17.0	39.6	17.0	39.6	8.1
22	21.7	26.4	21.7	26.4	8.1
23	21.7	26.4	9.4	22.6	8.1
24	21.7	26.4	9.4	20.7	8.1
25	21.7	26.4	21.7	25.5	8.1
26	9.4	39.6	9.4	30.2	8.1
27	9.4	35.8	9.4	33.9	8.1
28	9.4	28.3	9.4	33.9	8.1
29	21.7	26.4	17.0	35.8	8.1
30	18.9	26.4	9.4	33.9	8.1
31	9.4	33.9	9.4	33.9	8.1
32	9.4	30.2	9.4	33.9	8.1
33	9.4	32.1	9.4	33.9	8.1

Fig. 3. (a) Phase profile of the proposed hyper-dispersive metalens at the designed wavelength of $\lambda_0 = 118.8$ µm, where the red curve is the ideal hyperbolic phase distribution along the radial direction, and the red squares denote the actual discrete phase distribution. (b) Amplitude transmittance distribution along the radial direction at the designed wavelength. (c) GD of the proposed hyper-dispersive metalens. The red solid curve is the ideal GD, and the blue dots are actual GD provided by the 33 optimized meta-atoms. (d) GDD of the proposed hyper-dispersive metalens. The green solid curve is the ideal GDD, and the navy dots are actual GDD provided by the 33 optimized meta-atoms.

actual GDD curve shows a clear deviation from the ideal case, it has no significant influence on the dispersion property of the proposed hyper-dispersive metalens, because the phase contribution from the GDD item is much smaller than that of the GD item according to Eq. (2). The validity of this

approximation is verified in the following theoretical and experimental results.

The hyper-dispersion performance of the proposed metalens was first investigated for the two cases of actual and ideal dispersion (GD and GDD) distributions presented in Fig. 4,
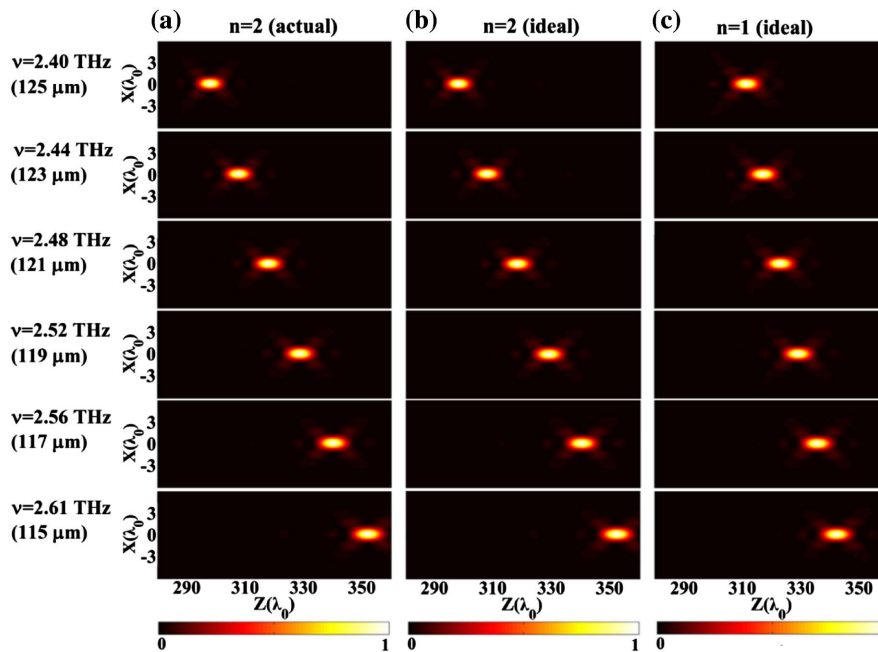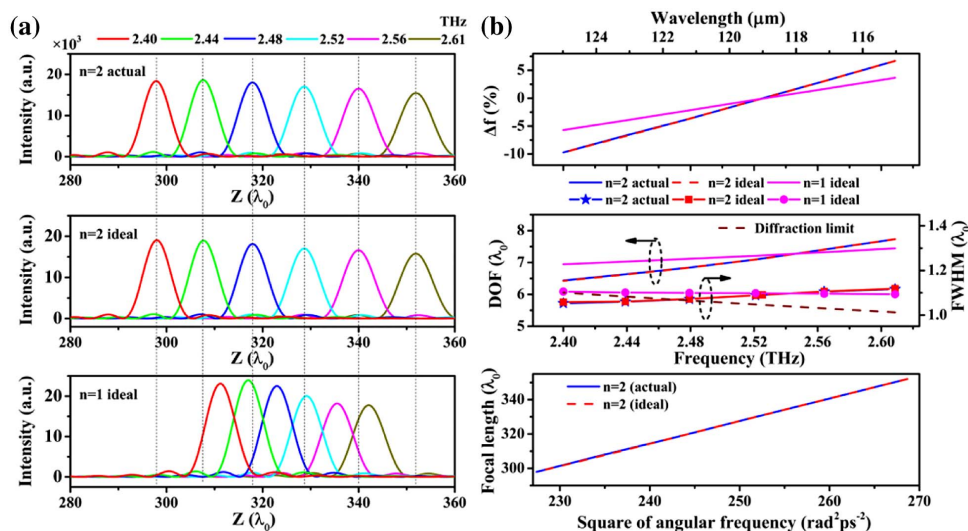

Fig. 4. Intensity distribution of focused optical field in the x–z plane at six different optical frequencies, i.e., 2.40, 2.44, 2.48, 2.52, 2.56, and 2.61 THz for (a) hyper-dispersive metalens with actual GD and GDD, (b) hyper-dispersive metalens with ideal GD and GDD, and (c) regular diffractive metalens.

respectively, by using the vector angular spectrum method (VASM) [53,54]. In the simulation, the actual GD and GDD distributions are achieved by the 33 optimized meta-atoms, and the ideal GD and GDD are the required values of the proposed hyper-dispersive metalens as presented in Figs. 3(c) and 3(d). In addition, both hyper-dispersive lenses possess the same phase profile at the design wavelength and the same amplitude transmittance distributions within the bandwidth provided by the meta-atoms. For comparison, a regular diffractive metalens ($n = 1$) was also designed with the same parameters, i.e., f_0 and R at the designed wavelength of λ_0, where the phase profile was provided by geometrical phase with the same meta-atom (#33). The intensity distribution of the focused optical field in the x–z plane is plotted at six different wavelengths with equal intervals in the wavelength range from 125 to 115 μm (i.e., from 2.40 to 2.61 THz) for the three cases of actual hyper-dispersive metalens ($n = 2$), ideal hyper-dispersive metalens ($n = 2$), and regular diffractive metalens ($n = 1$). It is clearly seen that the two hyper-dispersive metalenses exhibit stronger chromatic dispersion along the optical axis. As expected, there is no obvious difference found between the actual and ideal hyper-dispersive metalenses, as mentioned above. According to the simulation result, the focusing efficiency of the proposed hyper-dispersive metalens varies from 32.8% to 34.9% within the concerned wavelength range. With the development of artificial intelligence, deep learning can be utilized to inverse design meta-atoms in a data-driven manner, which can be a potential approach to improve focusing efficiency.

Figure 5(a) depicts the optical intensity distribution along the z axis for the two hyper-dispersive metalenses and the regular diffractive metalens. The results of the two hyper-dispersive metalenses are almost the same. The focal spot position varies from $Z = 297.91\lambda_0$ to $352.05\lambda_0$ ($54.14\lambda_0$) as the frequency increases from 2.40 to 2.61 THz (i.e., 125 to 115 μm).

There is a small variation about 17.3% in the focal spot intensity as the frequency changes. In the same frequency range, the focal spot position of the regular diffractive metalens has a comparatively small change of $30.88\lambda_0$ from $Z = 311.20\lambda_0$ to $342.08\lambda_0$, and the corresponding intensity shows a larger variation of about 22.4%. Figure 5(b) plots the major properties of the focused optical field for the three metalenses, including the normalized focal length shift $\Delta f = (f_{actual} - f_0)/f_0$ (top), depth-of-focus (DOF = λ/NA^2, middle), transverse full-width at half-maximum (FWHM, middle), and focal length as a function of square of angular frequency (bottom). It is clearly seen that the curves of the two hyper-dispersive metalenses are overlapped. For the hyper-dispersive metalenses, the normalized focal length shifts are about 16.4%, which is roughly 1.76 times greater than that of the regular diffractive metalens with Δf of 9.3%. Moreover, the focal lengths for these lenses change almost linearly with frequency. The DOFs of the hyper-dispersive metalenses vary between $6.4\lambda_0$ and $7.6\lambda_0$, while the DOF of the regular diffractive metalens varies from $6.9\lambda_0$ to $7.3\lambda_0$ within the concerned frequency range. The two hyper-dispersive metalenses have smaller DOFs in the wavelength range from 117.8 to 125 μm, indicating better axial resolution in most of the concerned wavelength range. The FWHMs of the hyper-dispersive metalenses vary from $1.12\lambda_0$ to $1.05\lambda_0$ within the concerned bandwidth. It is noted that the FWHM becomes smaller than the diffraction limit (dashed line) when the wavelength is larger than 121 μm. This is attributed to the fact that the amplitude transmittance in the center area of the lens becomes comparatively small and results in a high-pass filter, which helps to reduce the size of the focal spot [47]. The focal spot size of the regular diffractive metalens is diffraction limited for all simulated wavelengths, and the relative errors of the FWHM with respect to the regular diffractive metalens are 2.10%, 0.85%, –0.85%, –2.50%, –3.71%, and –4.75% at wavelengths of 115, 117, 119,


Fig. 5. (a) Optical intensity along the z axis at six different frequencies, i.e., 2.40, 2.44, 2.48, 2.52, 2.56, and 2.61 THz for the hyper-dispersive metalens with actual GD and GDD (top), hyper-dispersive metalens with ideal GD and GDD (middle), and regular diffractive metalens (bottom). (b) Normalized focal length shift (top), depth of focus (middle), and FWHM (middle) as a function of optical frequency for hyper-dispersive metalenses and regular diffractive metalens. The dashed line gives the corresponding diffraction limit. The bottom panel of (b) plots the focal length as a function of square angular frequency for hyper-dispersive metalenses.

121, 123, and 125 µm, respectively. In most of the concerned wavelength range, from 119 to 125 µm, the proposed hyper-dispersive metalenses have smaller FWHMs compared to the regular diffractive metalens, which results from the extra amplitude modulation. The chromatic dispersions of the two hyper-dispersive metalenses show the same behavior, and the corresponding value of A is 155.73 µm rad^{-2} ps^2, which is consistent with theoretical design.

3. EXPERIMENTAL RESULTS AND DISCUSSION

To experimentally verify the performance of the proposed hyper-dispersive metalens, a sample was fabricated by deep reactive ion etching (DRIE). In the fabrication, a silicon-on-insulator (SOI) wafer with a 65.7-µm-thick device layer and a 2-µm-thick buried oxide layer was employed, where the buried oxide layer acted as the etch-stop layer to guarantee large-area uniformity in the height of the meta-atoms. Despite the end reflection of the Si substrate, the buried oxide layer does not affect the performance of the hyper-dispersive metalens due to its much less thickness compared with the working wavelengths [16]. Figures 6(a) and 6(b) show an image of the entire metalens and a zoom-in image of the lens near its central area, where the scale bars represent a length of 60 µm.

Since linear polarization is a superposition of right-circular polarization and left-circular polarization (LCP) [8], its LCP component can be focused by the proposed hyper-dispersive metalens. In the experimental characterization, a quantum cascade laser (QCL) was used as a broadband coherent THz source [55], which emits linearly polarized light in a wavelength range from 114.5 to 120 µm. Figure 7(a) gives the emission spectrum of the THz QCL at a drive current of 950 mA, which contains five strong lines at frequencies of 2.52, 2.54, 2.56, 2.58, and 2.60 THz as marked in green circles. The experimental setup can be found in Fig. 7(b). The laser beam was first collimated by a 90° off-axis parabolic mirror with an effective focal length of 101.6 mm (MPD249-M01, Thorlabs Inc.). A linear polarizer was used to control the intensity of the wave incident on the metalens. A homemade THz blazed grating with a period of $1.15\lambda_0$ (at $\lambda_0 = 118.8$ µm) and depth of 30 µm was used to select frequency from the broadband emission by choosing the proper first-order diffraction. According to the finite time domain difference simulation, the diffraction efficiency of the grating varies from 45.0% to 47.2% within a frequency range from 2.48 to 2.62 THz. The corresponding resolved frequency interval is 15 GHz, which is effective for the used QCL with an approximate spectrum interval of 20 GHz. There is a balance between diffraction efficiency and the maximum etching depth
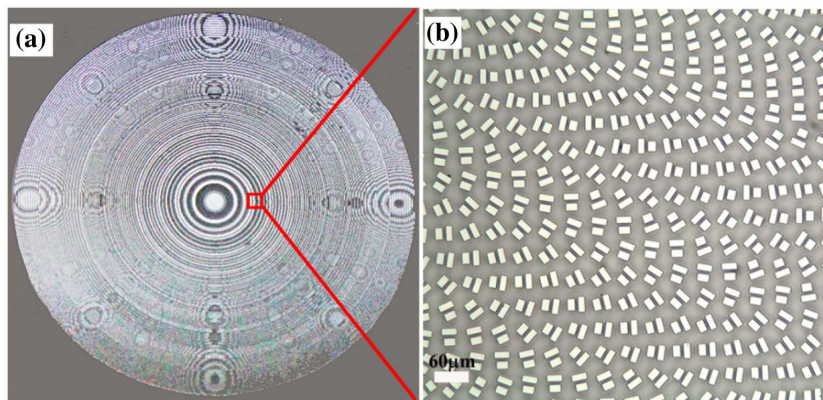
Fig. 6. (a) Image of the fabricated hyper-dispersive metalens. (b) Zoom-in image of the area marked by the red square in (a).
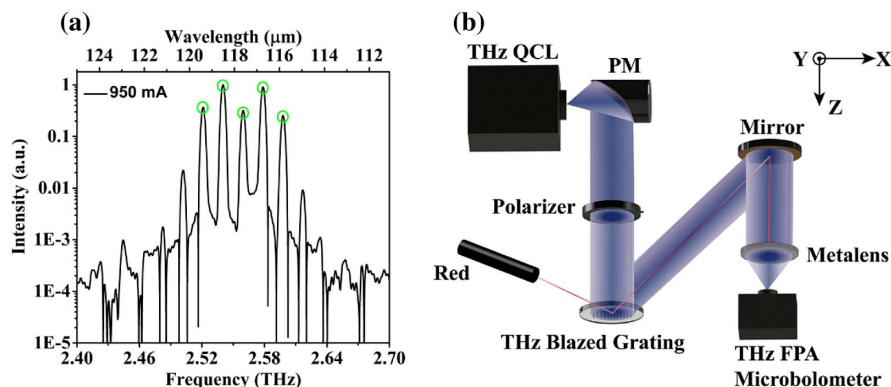
Fig. 7. (a) Emission spectra of the THz QCL at drive current of 950 mA. (b) Experimental setup for the hyper-dispersive metalens, where the homemade THz blazed grating is used to select illuminating wavelength from broadband laser emission by changing its rotation angle.
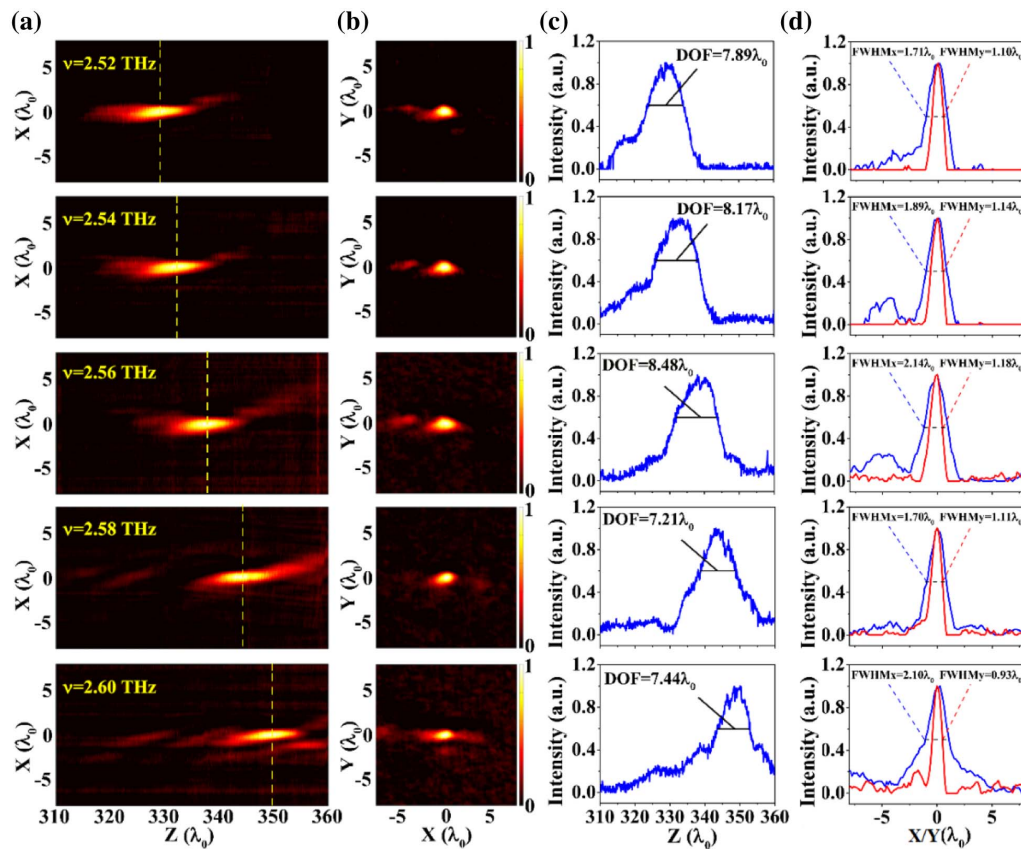
Fig. 8. Measured focused optical field at different frequencies of 2.52, 2.54, 2.56, 2.58, and 2.60 THz. (a) Normalized two-dimensional intensity distribution on the x–z plane. (b) Normalized two-dimensional intensity distribution on the focal planes, as marked by the dashed lines. (c) Intensity distribution along the z axis. (d) Intensity distribution along the x direction (blue) and y direction (red) crossing the centers of the focal spots, where FWHM_x and FWHM_y give the sizes of the focal spot in the x and y directions.

determined by the inherent angle of 54.7° of the anisotropic Si substrate. The collimated broadband THz beam incident on the THz blazed grating was diffracted in the x–z plane. The first-order diffraction beam was reflected by a mirror and illuminated the metalens from the substrate side, and the diffraction pattern behind the metalens was obtained directly by a THz focal-plane-array (FPA) microbolometer (Microcam 3 THz, Thermoteknix, UK) with a spatial resolution of 640×480 and pixel size of 17 μm × 17 μm. The microbolometer was mounted on a motorized three-dimensional translation stage (Z825B, Thorlabs Inc.), while the blazed grating and the mirror were mounted on the same rotation stage with an angle resolution of 5 arc min (PR01/M, Thorlabs Inc.). In the experiment, a red laser beam was used for optical alignment and to help determine the frequency of the selected THz wave.

Figure 8(a) gives the measured two-dimensional intensity profile of the focused field on the x–z plane for the five different frequencies, where the yellow-dashed lines denote the actual focal planes. As shown in the figure, the position of the focal spot varies from $329.28\lambda_0$ to $350.06\lambda_0$ as the frequency increases from 2.52 to 2.60 THz. The corresponding normalized two-dimensional intensity profiles on the focal planes are plotted in Fig. 8(b), which show clearly non-circular symmetry. This is caused by the obliquely incident waves from the grating

on the x–z plane [47]. Figures 8(c) and 8(d) show the intensity distribution along the z, x, and y axes on the corresponding focal planes for all tested wavelengths. The measured DOFs are $7.89\lambda_0$, $8.17\lambda_0$, $8.48\lambda_0$, $7.21\lambda_0$, and $7.44\lambda_0$ at frequencies of 2.52, 2.54, 2.56, 2.58, and 2.60 THz, while the theoretical values are $7.12\lambda_0$, $7.19\lambda_0$, $7.37\lambda_0$, $7.53\lambda_0$, and $7.68\lambda_0$, respectively. FWHM_x and FWHM_y denote the FWHM of focal spots in the x and y directions, respectively. The measured values of FWHM_x and FWHM_y are $1.71\lambda_0$ and $1.10\lambda_0$, $1.89\lambda_0$ and $1.14\lambda_0$, $2.14\lambda_0$ and $1.18\lambda_0$, $1.70\lambda_0$ and $1.11\lambda_0$, and $2.10\lambda_0$ and $0.93\lambda_0$ at frequencies of 2.52, 2.54, 2.56, 2.58, and 2.60 THz, respectively. It is noted that FWHM_y is close to its theoretical predication, $1.09\lambda_0$, $1.09\lambda_0$, $1.10\lambda_0$, $1.11\lambda_0$, and $1.11\lambda_0$, while FWHM_x shows a large deviation from its theoretical values, which is caused by the broadening of the spot size in the x direction resulting from the obliquely incident light at undesired frequencies [47].

To eliminate the influence of obliquely incident waves, the metalens was impinged by the collimated THz wave without using the THz blazed grating. Figure 9(a) gives the emission spectra of the QCL, where the QCL was operated in single longitudinal mode and multi-modes at currents of 650 and 950 mA, respectively. Figure 9(b) gives the corresponding normalized intensity distributions on the x–z propagation plane,
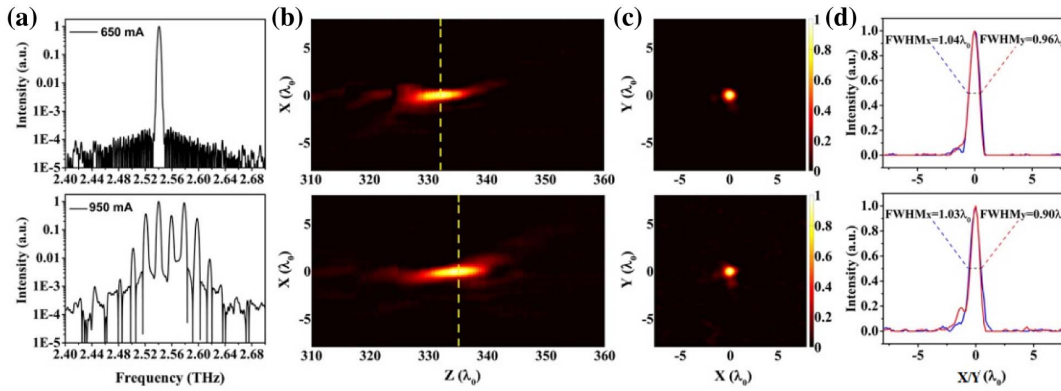
Fig. 9. (a) Emission spectra of the QCL working at 650 and 950 mA. (b) Measured optical intensity distributions along the propagation direction at different currents. (c) Optical intensity distributions on the actual focal plane (yellow dashed line). (d) Intensity distribution curves in the x and y directions crossing the centers of the spots in (c).
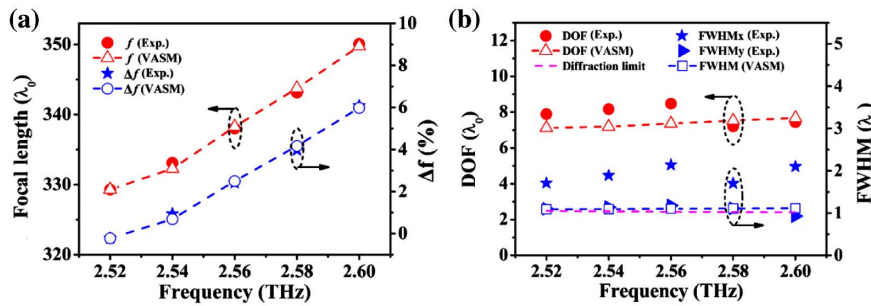
Fig. 10. Comparison between experimental and simulation results. (a) Measured focal length (red dots) is plotted against the optical frequency along with its simulation (red triangles) counterparts, and the normalized focal length shift Δf is plotted as a function of the frequency for experimental (blue stars) and simulation (blue circles) results. (b) Measured (red dots) depth of focus is plotted against the optical frequency, and its simulation result (red triangles) is presented for comparison. The focal spot sizes in the x (blue stars) and y (blue triangles) directions are given at frequencies of 2.52, 2.54, 2.56, 2.58, and 2.60 THz, and the simulated result (blue squares) is also plotted for comparison. The pink dashed line denotes the diffraction limit.

where the yellow dashed line denotes the actual focal plane. Figure 9(c) presents the optical intensity distributions on the focal plane, which show approximately circular symmetry in the optical intensity profiles. The corresponding intensity curves in x and y directions crossing the centers of the spots in Fig. 9(c) are also plotted in Fig. 9(d), and the FWHM values of the focal spots are $1.04\lambda_0$ and $0.96\lambda_0$, and $1.03\lambda_0$ and $0.90\lambda_0$, respectively.

Figure 10(a) plots the measured focal length (red dots) against the optical frequency, where the corresponding VASM results (red triangles) are also plotted for comparison. It is clearly seen that these results show very good agreement, indicating excellent hyper-dispersion performance of the proposed metalens. In Fig. 10(a), the normalized focal length shift is also plotted for the measured (blue stars) and VASM (blue circles) results, showing excellent agreement, as expected. Figure 10(b) gives the FWHM and DOF as functions of the optical frequency for the experiment and simulation results. The measured FWHM_y values are consistent with the theoretical results for all tested frequencies, while the corresponding FWHM_x values show a clear deviation from their simulated values due to the obliquely incident wave in the x–z plane

[47]. The measured FWHM_y is smaller than the corresponding diffraction limit (pink dashed line) only at a frequency of 2.60 THz, while it is above the diffraction limit for the other four tested frequencies. A slight discrepancy of the tested and simulated FWHM_y at a frequency of 2.6 THz may be caused by fabrication imperfections with an extra phase or amplitude modulation involved. The measured DOF has a fluctuation of 15.06% around the simulated results in the concerned frequency range.

4. CONCLUSION

We have demonstrated a hyper-dispersive metalens in the terahertz regime by simultaneously manipulating the phase, GD, and GDD. The proposed hyper-dispersive metalens has a radius of $180\lambda_0$ and numerical aperture of 0.478 at the designed wavelength of $\lambda_0 = 118.8$ μm. Simulation results show that the focal length shift is $54.14\lambda_0$ as the frequency increases from 2.40 to 2.61 THz, which is 1.76 times greater than that of a regular diffractive metalens with the same focal length of $f_0 = 330\lambda_0$ and radius of $180\lambda_0$ at the wavelength of λ_0. The measured focal length shift is $20.78\lambda_0$ as the frequency increases

from 2.52 to 2.60 THz. Both simulated and experimental results exhibit enhanced chromatic dispersion compared with the regular diffractive metalens. The simulation shows narrowing in the DOF of the hyper-dispersive lens compared to that of the regular diffractive metalens in most of the concerned bandwidth, implying an enhancement in axial spectrum resolution, which is important for spectral tomography. Moreover, a higher-order lens ($n > 2$) with large size, large numerical aperture, broad working bandwidth, and high focusing efficiency may be achieved in the future by improving fabrication technology or further optimizing the structural configuration by inverse design algorithms as well as overcoming the non-monotone variation of the high-order dispersion terms. One potential tomographic capability of hyper-dispersive metalenses, i.e., focal length tunability with respect to wavelength, has been demonstrated, and such hyper-dispersive metalenses can find numerous applications in spectroscopy and microscopy by utilizing the wavelength as a tuning dimension.

Disclosures. The authors declare no conflicts of interest.

Data Availability. The data that support the findings of this study are not publicly available at this time but may be obtained from the authors upon reasonable request.

†These authors contributed equally to this paper.

REFERENCES

1. H. J. Tiziani and H. M. Uhde, "Three-dimensional image sensing by chromatic confocal microscopy," Appl. Opt. **33**, 1838–1843 (1994).
2. B. S. Chun, K. Kim, and D. Gweon, "Three-dimensional surface profile measurement using a beam scanning chromatic confocal microscope," Rev. Sci. Instrum. **80**, 73706 (2009).
3. K. Shi, P. Li, S. Yin, and Z. Liu, "Chromatic confocal microscopy using supercontinuum light," Opt. Express **12**, 2096–2101 (2004).
4. S. L. Dobson, P. C. Sun, and Y. Fainman, "Diffractive lenses for chromatic confocal imaging," Appl. Opt. **36**, 4744–4748 (1997).
5. S. Wang, B. Ferguson, D. Abbott, and X. C. Zhang, "T-ray imaging and tomography," J. Biol. Phys. **29**, 247–256 (2003).
6. X. Ni, N. K. Emani, A. V. Kildishev, A. Boltasseva, and V. M. Shalaev, "Broadband light bending with plasmonic nanoantennas," Science **335**, 427 (2012).
7. C. Chen, W. Song, J. Chen, J. Wang, Y. H. Chen, B. Xu, M. Chen, H. Li, B. Fang, J. Chen, H. Y. Kuo, S. Wang, D. P. Tsai, S. Zhu, and T. Li, "Spectral tomographic imaging with aplanatic metalens," Light Sci. Appl. **8**, 99 (2019).
8. X. Jiang, H. Chen, Z. Li, H. Yuan, L. Cao, Z. Luo, K. Zhang, Z. Zhang, Z. Wen, L. Zhu, X. Zhou, G. Liang, D. Ruan, L. Du, L. Wang, and G. Chen, "All-dielectric metalens for terahertz wave imaging," Opt. Express **26**, 14132–14142 (2018).
9. F. Aieta, M. A. Kats, P. Genevet, and F. Capasso, "Multiwavelength achromatic metasurfaces by dispersive phase compensation," Science **347**, 1342–1345 (2015).
10. X. Xie, X. Li, M. Pu, X. Ma, K. Liu, Y. Guo, and X. Luo, "Plasmonic metasurfaces for simultaneous thermal infrared invisibility and holographic illusion," Adv. Funct. Mater. **28**, 1706673 (2018).
11. A. C. Overvig, S. Shrestha, S. C. Malek, M. Lu, A. Stein, C. Zheng, and N. Yu, "Dielectric metasurfaces for complete and independent control of the optical amplitude and phase," Light Sci. Appl. **8**, 92 (2019).
12. Q. Zhang, F. Dong, H. Li, Z. Wang, G. Liang, Z. Zhang, Z. Wen, Z. Shang, G. Chen, L. Dai, and W. Chu, "High-numerical-aperture dielectric metalens for super-resolution focusing of oblique incident light," Adv. Opt. Mater. **8**, 1901885 (2020).
13. S. Tian, H. Guo, J. Hu, and S. Zhuang, "Dielectric longitudinal bifocal metalens with adjustable intensity and high focusing efficiency," Opt. Express **27**, 680–688 (2019).
14. L. Huang, X. Chen, H. Mühlenbernd, G. Li, and S. Zhang, "Dispersionless phase discontinuities for controlling light propagation," Nano Lett. **12**, 5750–5755 (2012).
15. Y. Nanfang, G. Patrice, M. A. Kats, A. Francesco, T. Jean-Philippe, C. Federico, and G. Zeno, "Light propagation with phase discontinuities: generalized laws of reflection and refraction," Science **334**, 333–337 (2011).
16. H. Chen, Z. Wu, Z. Li, Z. Luo, X. Jiang, Z. Wen, L. Zhu, X. Zhou, H. Li, Z. Shang, Z. Zhang, K. Zhang, G. Liang, S. Jiang, L. Du, and G. Chen, "Sub-wavelength tight-focusing of terahertz waves by polarization-independent high-numerical-aperture dielectric metalens," Opt. Express **26**, 29817–29825 (2018).
17. J. P. Balthasar Mueller, N. A. Rubin, R. C. Devlin, B. Groever, and F. Capasso, "Metasurface polarization optics: independent phase control of arbitrary orthogonal states of polarization," Phys. Rev. Lett. **118**, 113901 (2017).
18. R. Zuo, W. Liu, H. Cheng, S. Chen, and J. Tian, "Breaking the diffraction limit with radially polarized light based on dielectric metalenses," Adv. Opt. Mater. **6**, 1800795 (2018).
19. F. Ding, Z. Wang, S. He, V. M. Shalaev, and A. V. Kildishev, "Broadband high-efficiency half-wave plate: a supercell-based plasmonic metasurface approach," ACS Nano **9**, 4111–4119 (2015).
20. C. Pfeiffer, C. Zhang, V. Ray, L. Jay Guo, and A. Grbic, "Polarization rotation with ultra-thin bianisotropic metasurfaces," Optica **3**, 427–432 (2016).
21. Z. Wu, F. Dong, S. Zhang, S. Yan, G. Liang, Z. Zhang, Z. Wen, G. Chen, L. Dai, and W. Chu, "Broadband dielectric metalens for polarization manipulating and superoscillation focusing of visible light," ACS Photon. **7**, 180–189 (2019).
22. M. J. Escuti, M. W. Kudenov, and J. Kim, "Controlling light with geometric-phase holograms," Opt. Photon. News **27**, 22–29 (2016).
23. P. Chen, B. Fang, J. Li, M. Kong, and Z. Hong, "Enhancement of efficiency on the Pancharatnam–Berry geometric phase metalens in the terahertz region," Appl. Opt. **60**, 7849–7857 (2021).
24. H. Zhang, X. Zhang, Q. Xu, C. Tian, Q. Wang, Y. Xu, Y. Li, J. Gu, Z. Tian, C. Ouyang, X. Zhang, C. Hu, J. Han, and W. Zhang, "High-efficiency dielectric metasurfaces for polarization-dependent terahertz wavefront manipulation," Adv. Opt. Mater. **6**, 1700773 (2017).
25. H. Zhao, X. Wang, J. He, J. Guo, J. Ye, Q. Kan, and Y. Zhang, "High-efficiency terahertz devices based on cross-polarization converter," Sci. Rep. **7**, 17882 (2017).
26. L. Yin, T. Huang, D. Wang, J. Liu, Y. Sun, and P. Liu, "Terahertz dual phase gradient metasurfaces: high-efficiency binary-channel spoof surface plasmon excitation," Opt. Lett. **45**, 411–414 (2020).
27. B. Yao, X. Zang, Z. Li, L. Chen, J. Xie, Y. Zhu, and S. Zhuang, "Dual-layered metasurfaces for asymmetric focusing," Photon. Res. **8**, 830–843 (2020).
28. R. Wang, J. Han, J. Liu, H. Tian, W. Sun, L. Li, and X. Chen, "Multi-foci metalens for terahertz polarization detection," Opt. Lett. **45**, 3506–3509 (2020).

29. J. He, J. Ye, X. Wang, Q. Kan, and Y. Zhang, "A broadband terahertz ultrathin multi-focus lens," Sci. Rep. **6**, 28800 (2016).

30. W. Pan and J. Li, "Diversified functions for a terahertz metasurface with a simple structure," Opt. Express **29**, 12918–12929 (2021).

31. J. Li and L. Yang, "Transmission and reflection bi-direction terahertz encoding metasurface with a single structure," Opt. Express **29**, 33760–33770 (2021).

32. B. Xiao, Y. Zhang, S. Tong, J. Yu, and L. Xiao, "Novel tunable graphene-encoded metasurfaces on an uneven substrate for beam-steering in far-field at the terahertz frequencies," Opt. Express **28**, 7125–7138 (2020).

33. M. Zhang, F. Zhang, Y. Ou, J. Cai, and H. Yu, "Broadband terahertz absorber based on dispersion-engineered catenary coupling in dual metasurface," Nanophotonics **8**, 117–125 (2018).

34. T. Ma, K. Nallapan, H. Guerboukha, and M. Skorobogatiy, "Analog signal processing in the terahertz communication links using waveguide Bragg gratings: example of dispersion compensation," Opt. Express **25**, 11009–11026 (2017).

35. S. Qu, W. Wu, B. Chen, H. Yi, X. Bai, K. B. Ng, and C. H. Chan, "Controlling dispersion characteristics of terahertz metasurface," Sci. Rep. **5**, 9367 (2015).

36. Y. Zhao and A. Alù, "Tailoring the dispersion of plasmonic nanorods to realize broadband optical meta-waveplates," Nano Lett. **13**, 1086–1091 (2013).

37. T. C. Wei, Y. Z. Alexander, and C. Federico, "Flat optics with dispersion-engineered metasurfaces," Nat. Rev. Mater. **5**, 604–620 (2020).

38. J. Sisler, W. T. Chen, A. Y. Zhu, and F. Capasso, "Controlling dispersion in multifunctional metasurfaces," APL Photon. **5**, 56107 (2020).

39. W. Zang, Q. Yuan, R. Chen, L. Li, T. Li, X. Zou, G. Zheng, Z. Chen, S. Wang, and Z. Wang, "Chromatic dispersion manipulation based on metalenses," Adv. Mater. **32**, 1904935 (2020).

40. S. Wang, P. C. Wu, V. C. Su, Y. C. Lai, M. K. Chen, H. Y. Kuo, B. H. Chen, Y. H. Chen, T. T. Huang, and J. H. Wang, "A broadband achromatic metalens in the visible," Nat. Nanotechnol. **13**, 227–232 (2018).

41. W. T. Chen, A. Y. Zhu, V. Sanjeev, M. Khorasaninejad, Z. Shi, E. Lee, and F. Capasso, "A broadband achromatic metalens for focusing and imaging in the visible," Nat. Nanotechnol. **13**, 220–226 (2018).

42. W. T. Chen, A. Y. Zhu, J. Sisler, Z. Bharwani, and F. Capasso, "A broadband achromatic polarization-insensitive metalens consisting of anisotropic nanostructures," Nat. Commun. **10**, 355–362 (2019).

43. A. Arbabi, A. Faraon, E. Arbabi, S. M. Kamali, and H. Yu, "Controlling the sign of chromatic dispersion in diffractive optics with dielectric metasurfaces," Optica **4**, 625–632 (2017).

44. S. Wang, P. C. Wu, V. C. Su, Y. C. Lai, C. H. Chu, J. W. Chen, S. H. Lu, J. Chen, B. Xu, and C. H. Kuan, "Broadband achromatic optical metasurface devices," Nat. Commun. **8**, 187–195 (2017).

45. S. Shrestha, A. C. Overvig, M. Lu, A. Stein, and N. Yu, "Broadband achromatic dielectric metalenses," Light Sci. Appl. **7**, 85–96 (2018).

46. Q. Cheng, M. Ma, D. Yu, Z. Shen, J. Xie, J. Wang, N. Xu, W. Hu, S. Wang, T. Li, and S. Zhuang, "Broadband achromatic metalens in terahertz regime," Sci. Bull. **64**, 1525–1531 (2019).

47. F. Zhao, Z. Li, X. Dai, X. Liao, S. Li, J. Cao, Z. Shang, Z. Zhang, G. Liang, G. Chen, H. Li, and Z. Wen, "Broadband achromatic sub-diffraction focusing by an amplitude-modulated terahertz metalens," Adv. Opt. Mater. **8**, 2000842 (2020).

48. Z. Jin, D. Janoschka, J. Deng, L. Ge, P. Dreher, B. Frank, G. Hu, J. Ni, Y. Yang, J. Li, C. Yu, D. Lei, G. Li, S. Xiao, S. Mei, H. Giessen, F. M. Zu Heringdorf, and C. Qiu, "Phyllotaxis-inspired nanosieves with multiplexed orbital angular momentum," eLight **1**, 5 (2021).

49. E. Maguid, I. Yulevich, D. Veksler, V. Kleiner, M. L. Brongersma, and E. Hasman, "Photonic spin-controlled multifunctional shared-aperture antenna array," Science **352**, 1202–1206 (2016).

50. V. R. Almeida, Q. Xu, C. A. Barrios, and M. Lipson, "Guiding and confining light in void nanostructure," Opt. Lett. **29**, 1209–1211 (2004).

51. F. Zhao, X. Jiang, S. Li, H. Chen, G. Liang, Z. Wen, Z. Zhang, and G. Chen, "Optimization-free approach for broadband achromatic metalens of high-numerical-aperture with high-index dielectric metasurface," J. Phys. D **52**, 505110 (2019).

52. J. Zhou, H. Qian, G. Hu, H. Luo, S. Wen, and Z. Liu, "Broadband photonic spin Hall meta-lens," ACS Nano **12**, 82–88 (2018).

53. J. Goodman, *Introduction to Fourier Optics* (Electronic Industry, 1968).

54. Z. Wu, Q. Zhang, X. Jiang, Z. Wen, G. Liang, Z. Zhang, Z. Shang, and G. Chen, "Broadband integrated metalens for creating super-oscillation 3D hollow spot by independent control of azimuthally and radially polarized waves," J. Phys. D **52**, 415103 (2019).

55. H. Li, J. M. Manceau, A. Andronico, V. Jagtap, C. Sirtori, L. H. Li, E. H. Linfield, A. G. Davies, and S. Barbieri, "Coupled-cavity terahertz quantum cascade lasers for single mode operation," Appl. Phys. Lett. **104**, 241102 (2014).